

Parametric Light-Matter Interaction in the Single-Photon Strong Coupling Limit

C.A. Potts*, R.C. Dekker, S. Deve, E.W. Strijbis, G.A. Steele†

Kavli Institute of Nanoscience, Delft University of Technology, PO Box 5046, 2600 GA Delft, The Netherlands

*Email: c.a.potts@tudelft.nl

†Email: g.a.steele@tudelft.nl

Parametric coupling between harmonic oscillators has enabled exquisite measurement precision and control of linear resonators, being extensively studied, for example, in cavity optomechanics. This level of control has been made possible by using strong sideband drives, enhancing the coupling rate while also linearizing the interaction. In this article, we demonstrate a new paradigm of parametrically coupled microwave circuits replacing one *linear* microwave cavity with a superconducting transmon qubit. Our system utilizes photon-pressure coupling between the transmon qubit and a highly linear microwave resonator, a microwave analog of the radiation-pressure interaction. Applying a strong sideband drive results in an on-demand, non-linear Jaynes-Cummings interaction with the linear resonator. We also observe a single-photon coupling rate an order of magnitude larger than all decay rates, placing the device in the single-photon strong coupling regime. This demonstration of photon-pressure Jaynes-Cummings interactions paves the way for developing novel photon-pressure quantum information processing hardware and will enable exotic tests of quantum gravity in the future by interfacing this new platform with mechanical resonators.

INTRODUCTION

Parametrically enhanced interactions between harmonic oscillators have provided the foundation for countless groundbreaking experiments in the last several decades. The canonical example is that of cavity optomechanics¹ but includes related fields such as cavity magnomechanics^{2–5}, photon-pressure coupling^{6–10}, and the center of mass motion of trapped ions¹¹. Such parametric interactions have enabled scientific achievements such as ground-state cooling of mechanical objects^{12–14}, the generation of deterministic mechanical entanglement¹⁵, microwave-to-optical frequency conversion^{16,17}, quantum non-demolition measurements^{18,19}, and many others. These demonstrations have relied on enhancing the typically small coupling rate via strong sideband drive tones, effectively linearizing the intrinsically nonlinear interaction, limiting its utility since, for example, linear interactions alone cannot be used to generate arbitrary quantum states²⁰.

The limitations of linear interactions can be avoided by using a non-linear element, such as a superconducting qubit. In conventional circuit quantum electrodynamics (cQED)²¹, a linear dipolar coupling results in the non-linear Jaynes-Cummings interaction. In this case, the circuit geometry determines the dipolar coupling rate, and the coupling cannot be controlled *in-situ*. Controlling the interaction can be achieved by shifting the qubit's frequency in and out of resonance^{22,23} or by implementing tunable coupling circuits between elements^{24,25}. However, even when detuned, the dipolar Jaynes-Cummings interaction results in residual dispersive coupling between circuit elements²¹. This parasitic coupling limits qubit-qubit gate fidelity²⁶ and limits the ability to strongly drive the linear circuit, which is crucial for integrating superconducting qubits with optomechanical devices.

In this article, we overcome these limitations of con-

ventional cQED by using photon-pressure coupling^{6,7} between a superconducting qubit and a linear microwave resonator circuit. The interaction between the qubit and the resonator is engineered by threading the magnetic flux generated by the linear resonator through a superconducting quantum interference device (SQUID), forming the inductance of the qubit. We observe parametric strong coupling between the qubit and the resonator with, on average, less than a single sideband drive photon. This provides dynamic control of a photon-pressure induced Jaynes-Cummings interaction with a high on-off ratio in a paradigm we refer to as photon-pressure cQED. Furthermore, the AC-Stark shift of the qubit provides an absolute photon number calibration²⁷, allowing for the extraction of the single-photon coupling rate. We find a single-photon coupling rate, $g_0 = 2\pi \times 11.9$ MHz, two orders of magnitude larger than the largest dissipation rate of the system, placing our system in the single-photon strong coupling regime, attained for the first time here.

In addition to representing a novel implementation of cQED, this architecture has exciting potential as a new platform for superconducting quantum information processing²⁸. Since there is negligible direct interaction between the qubit and the linear circuit in the absence of the sideband drive, it may be possible to couple multiple qubits to a single bus resonator, allowing all-to-all qubit connectivity, enabling highly efficient quantum error correction codes²⁹ and multi-qubit gates³⁰.

Moreover, the single-photon strong coupling regime has long been sought as it fully utilizes the inherent nonlinearity of the parametric interaction^{31,32}. Since linear interactions can only perform bilinear operations on Gaussian states, single-photon strong coupling would allow the dissipative engineering of states with Wigner negativity, such as described in the protocol for the generation of Schrödinger cat-states²⁰.

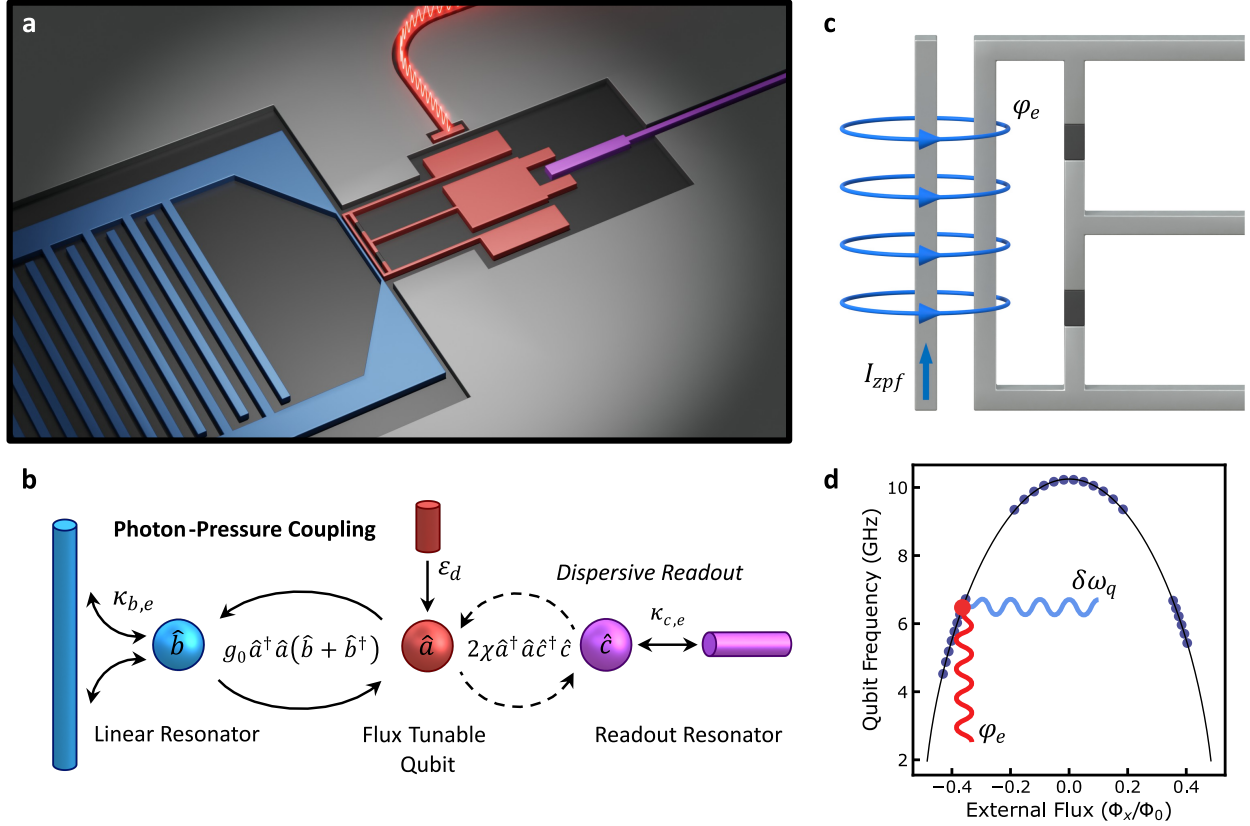


FIG. 1. Photon-pressure circuit and parametric coupling mechanism. **a**, A rendering of the photon-pressure device. **b**, Schematic diagram of the photon-pressure device. The qubit \hat{a} is coupled via photon-pressure to the linear resonator \hat{b} and coupled capacitively to a CPW resonator \hat{c} . **c**, Schematic depiction of the photon-pressure coupling mechanism. Zero-point current in the linear resonator generates a magnetic flux that modulates the qubit frequency. **d**, Qubit frequency as a function of the external magnetic flux, blue circles are experimental data, and the black line is a fit. The qubit has a sweet spot frequency of 10.2 GHz. The magnetic flux generated by currents in the linear resonator modulates the qubit frequency, resulting in photon-pressure coupling.

The photon-pressure induced Jaynes-Cummings interaction shown here will also enable the generation of arbitrary quantum states within the linear circuit²³. Furthermore, the qubit decouples from the linear resonator when the sideband drive is switched off, enabling a large number of photons to be driven into the linear resonator, unlike conventional Jaynes-Cummings cQED. Combining photon-pressure cQED with conventional optomechanics integrated within the linear resonator will enable the generation of mechanical Schrödinger cat states to explore gravity's effect on quantum mechanics³³.

DEVICE DESIGN

The device consists of our modified transmon qubit coupled to two superconducting resonators, all with frequencies in the gigahertz range. The device's full circuit schematic can be seen in Fig. 1. All circuits are fabricated from niobium-titanium nitride; the fabrication details are outlined in the methods section. A $\lambda/2$ co-planar waveguide resonator (CPW) labelled \hat{c} is capacitively coupled to the qubit and acts as a standard readout resonator for

qubit measurements and state preparation^{21,34}. It has a frequency $\omega_c = 2\pi \times 7.612$ GHz, a qubit-photon coupling rate $g_{ac} = 2\pi \times 118$ MHz, an internal and external coupling rate of $\kappa_{int,c} = 2\pi \times 72.8$ kHz and $\kappa_{ext,c} = 2\pi \times 673.8$ kHz.

The linear resonator labelled \hat{b} consists of a large interdigitated capacitor (IDC) shunted with a thin inductor wire. The linear resonator has a resonance frequency $\omega_b = 2\pi \times 4.347$ GHz, an internal and external coupling rate of $\kappa_{int,b} = 2\pi \times 28.0$ kHz and $\kappa_{ext,b} = 2\pi \times 88.6$ kHz and a residual parasitic dipolar coupling to the qubit $g_{ab} = 2\pi \times 2.5$ MHz. The parasitic capacitive coupling was minimized by careful qubit design and results in a critical photon number at the qubit operational point of $n_{crit} \equiv \Delta^2/4g_{ab}^2 \approx 125\,000$, where Δ is the qubit-linear resonator detuning³⁴. The reduced hybridization between the qubit and linear resonator is a novel feature of the photon-pressure qubit design; the low coupling rate g_{ab} allows relatively large coherent drives to be applied to the linear resonator. We observe a bare-to-dressed transition of the linear resonator with a steady state drive

$|\langle \hat{b} \rangle|^2 \approx 20\,000$, which is approximately an order of magnitude smaller than the critical photon number. However, we expect the number of drive photons to greatly increase even with moderate reductions of the parasitic dipolar coupling³⁵. These large coherent drives will be important if the linear resonator is replaced with a cavity optomechanical device since large coherent tones are required for mechanical state manipulation¹³.

Finally, the qubit labelled \hat{a} is a modified pocket-style transmon qubit with Manhattan-style aluminum/aluminum-oxide Josephson junctions³⁶. As seen in Fig. 1, one of the capacitor pads of the transmon is split and wrapped around the other, and the SQUID loop is extended away from the capacitor pads. The SQUID loop is placed $\sim 1\,\mu\text{m}$ from the thin inductor wire of the linear circuit. This design was implemented to reduce the electric dipole moment of the qubit, minimizing the parasitic dipole coupling to the linear resonator, as discussed previously. Currently, we believe the parasitic coupling likely results from junction asymmetry and charging of the surrounding ground plane.

A coil mounted below the sample provides an external magnetic field that can tune the frequency of the qubit; see Fig. 1(d). During this work, the qubit was operated at a frequency $\omega_q(\Phi_e) \sim 2\pi \times 6.10$ GHz, where Φ_e is the static external magnetic flux thread through the SQUID. The qubit can be driven via a direct XY-drive line, which was designed to be weakly coupled such that the Purcell limited linewidth $\kappa_{\text{pur}} \ll \gamma_q$, the qubit linewidth. Finally, we measured a T_2^* limited linewidth $\gamma_q = 2\pi \times 677$ kHz; qubit characterization is described within the supplementary information. The chip is mounted on the baseplate of a commercial dilution refrigerator operating with a base temperature of $T \sim 15$ mK. For details about the measurement and set-up, see the methods section.

OPERATION PRINCIPLE

We model the qubit as a Kerr oscillator with a large anharmonicity³⁴, the bare Hamiltonian of the system can be written in the form,

$$\hat{H}_0/\hbar = \omega_q(\Phi_e)\hat{a}^\dagger\hat{a} + \frac{\alpha}{2}\hat{a}^\dagger\hat{a}^\dagger\hat{a}\hat{a} + \omega_b\hat{b}^\dagger\hat{b}. \quad (1)$$

Here, $\alpha = -388$ MHz is the qubit anharmonicity at the operation point, $\hat{a}^{(\dagger)}$ and $\hat{b}^{(\dagger)}$ are the qubit and linear resonator annihilation (creation) operators, respectively.

Current flowing through the inductor wire of the linear resonator generates an oscillating magnetic flux through the SQUID loop, modulating the qubit's frequency and inducing the parametric photon-pressure coupling between the qubit and linear resonator, see Fig. 1(c,d). It can be shown, after some algebraic manipulation and keeping only first-order terms — see the supplementary information — that the interaction can be written in the simple form,

$$\hat{H}_{\text{int}}/\hbar = g_0\hat{a}^\dagger\hat{a}(\hat{b} + \hat{b}^\dagger). \quad (2)$$

Here, g_0 is the single-photon coupling rate and is given

by

$$g_0 = \frac{\partial\omega_q}{\partial\Phi}\Phi_{\text{zpf}}, \quad (3)$$

where $\partial\omega_q/\partial\Phi$ is the qubit's flux sensitivity at the operational point, and Φ_{zpf} is the magnetic flux thread through the SQUID loop generated by the zero-point current fluctuations of the linear resonator. The zero-point flux can be estimated from the mutual inductance and the zero-point fluctuations in the current given by $I_{\text{zpf}} = \sqrt{\hbar\omega_b/2L_b} \approx 36.8$ nA; with $\Phi_{\text{zpf}} = MI_{\text{zpf}}$. The mutual inductance can be estimated via the Biot-Savart law and gives $M \approx 25.9$ pH; therefore, we estimate the zero-point magnetic flux to have a value $\Phi_{\text{zpf}} \approx 461\,\mu\Phi_0$. We have normalized the magnetic flux in units of $\Phi_0 = h/(2e)$. At the qubit operational point, the flux sensitivity $\partial\omega_q/\partial\Phi = 2\pi \times 26.0$ GHz, thus we can estimate the single-photon coupling rate to have a value $g_0 \approx 2\pi \times 12.0$ MHz.

PHOTON-PRESSURE JAYNES-CUMMINGS

The photon-pressure Jaynes-Cummings interaction was implemented using a sideband drive tone tuned to the difference frequency between the two coupled oscillators.

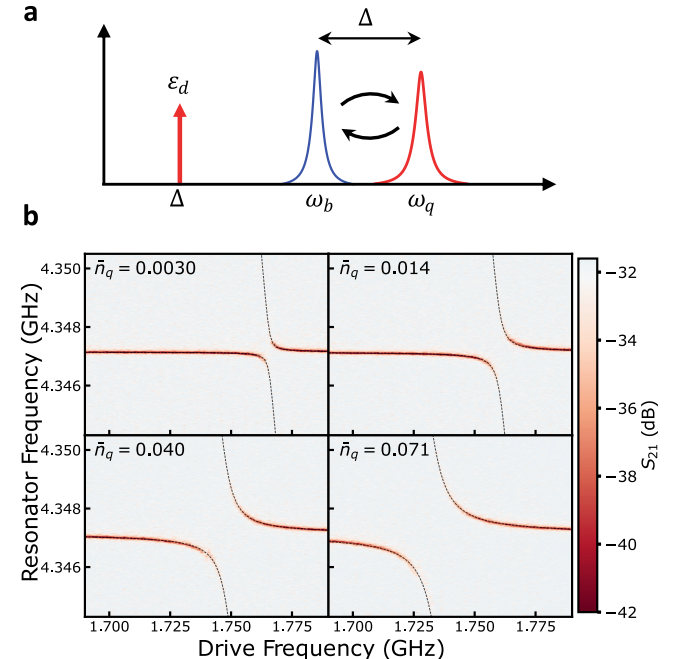


FIG. 2. Strong photon-pressure coupling. **a**, Schematic diagram of the relative frequencies of the qubit (red), the linear resonator (blue), and the sideband drive (red). **b**, The measured avoided level crossings of the linear resonator as a function of the sideband drive frequency. Starting from the top left, the drive powers considered here were $P_{\text{sb}} = 3.3, 8.3, 12.3, 14.4$ dBm, set at the source. The calibrated average number of sideband photons is printed in the top left of each panel. The dashed line is a fit; see the supplementary information for details.

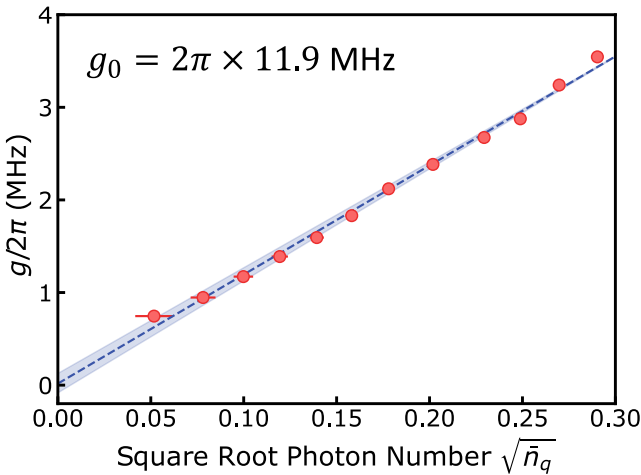


FIG. 3. **Single-photon coupling rate.** a, Photon-pressure coupling rates extracted from the normal mode spectra at different sideband drive powers. The coupling rates are plotted as a function of the square root sideband photon number. The red points are data, and the blue dashed line is a linear fit to the data. The blue shaded area considered the deviation due to the uncertainty in the non-Stark shifted qubit’s frequency. The photon number was calibrated using the AC-Stark shift.

tors; see Fig. 2(a). In cavity optomechanics, the sideband drive is typically nearly resonant with the optical cavity, as mechanical frequencies are 1-10 MHz for most electromechanical systems^{12,14}. However, photon-pressure cQED operates in a vastly different parameter regime. The sideband drive frequency is below both the qubit and linear resonator frequencies. We should emphasize that we are driving single-photon sideband transitions and *not* the two-photon sideband transitions used in Jaynes-Cummings cQED³⁷.

We can linearize the Hamiltonian about the sideband drive tone with frequency $\omega_d \approx \omega_q - \omega_b$ tuned near the red sideband³⁸ applied via the XY-drive line to the qubit. In a displaced frame co-rotating with the drive, we can linearize by defining $\hat{a} = \langle \hat{a} \rangle + \delta\hat{a}$; doing so, we can define the enhanced coupling rate as $g = g_0|\langle \hat{a} \rangle|$, and $\bar{n}_q = |\langle \hat{a} \rangle|^2$ is the average sideband steady-state population of the qubit. The interaction Hamiltonian given in Eq. 2 can be written, taking the two-level approximation of the transmon and applying the rotating wave approximation, as

$$\hat{\mathcal{H}}_{\text{int}}/\hbar = g(\hat{\sigma}_- \hat{b}^\dagger + \hat{\sigma}_+ \hat{b}), \quad (4)$$

where $\hat{\sigma}_\pm$ are the qubit raising and lowering operators. The linearization process results in a photon-pressure Jaynes-Cummings interaction created by the sideband drive; see the supplementary information for a full derivation.

The interaction is experimentally investigated by sweeping a strong sideband drive near the red sideband and probing the linear resonator with less than a single photon on average to remain in the single-excitation

manifold of the Jaynes-Cummings ladder³⁹. We observe a series of avoided level crossings with a correspondingly increasing coupling rate as a function of increasing sideband power and a shift to lower frequencies, as shown in Fig. 2(b). We can extract the cavity-enhanced coupling rate g from the avoided level crossings. However, we require an absolute calibration of the photon number to determine the single-photon coupling rate. Conventionally, this is achieved by varying the temperature of the dilution refrigerator and performing thermal calibration¹², or applying a known modulation and carefully measuring all loss and gain within the system^{40,41}.

Instead, here we can use the AC-Stark shift of the qubit for direct photon number calibration. As we increase the sideband drive power, the qubit experiences an increasing AC-Stark shift. The magnitude of the Stark shift is directly related to the average number of sideband photons in the qubit. One must take care when interpreting the Stark shift, which is why we initially modelled the qubit as a Kerr oscillator. Since the sideband drive is far detuned, the counter-rotating terms, known as the Bloch-Siegert shift²⁷, and the qubit anharmonicity contribute significantly. Considering the steady state of the Kerr oscillator and the AC-Stark shift, the steady-state qubit population for each sideband power can be directly calculated.

The value of the single-photon coupling rate can be determined by considering the cavity-enhanced coupling rate as a function of the square root of the number of steady-state sideband photons, as seen in Fig. 3. Importantly, the relationship is linear, suggesting our approximations are valid and hold even for steady-state populations below the single photon level, and the data has a y-intercept of zero, which is expected since the cavity-enhanced coupling should vanish for no sideband drive. The value of the single-photon coupling rate can be determined from the slope, giving a value of $g_0 = 2\pi \times 11.9 \pm 0.3$ MHz, which is in excellent agreement with our theoretical prediction and well within the single-photon strong coupling regime.

RABI OSCILLATIONS

Finally, to demonstrate the coherent nature of the photon-pressure interaction, we measure vacuum Rabi oscillations between the qubit and the linear resonator. The qubit is first prepared into its excited state $|e\rangle$ using a 24 ns resonant π -pulse. A square wave sideband pulse is applied near the red-sideband frequency for a variable time τ . Following the sideband pulse, the qubit state is measured using the capacitively coupled CPW resonator. This protocol is repeated for various sideband drive frequencies and pulse durations, resulting in the vacuum Rabi oscillations shown in Fig. 4. We observe a typical Rabi “chevron” pattern with coherent exchanges between the qubit and the linear resonator. A line cut is fit using a numerical simulation of the Rabi oscillations to confirm our linear model; see the methods section. From the numerical simulation, we can ex-

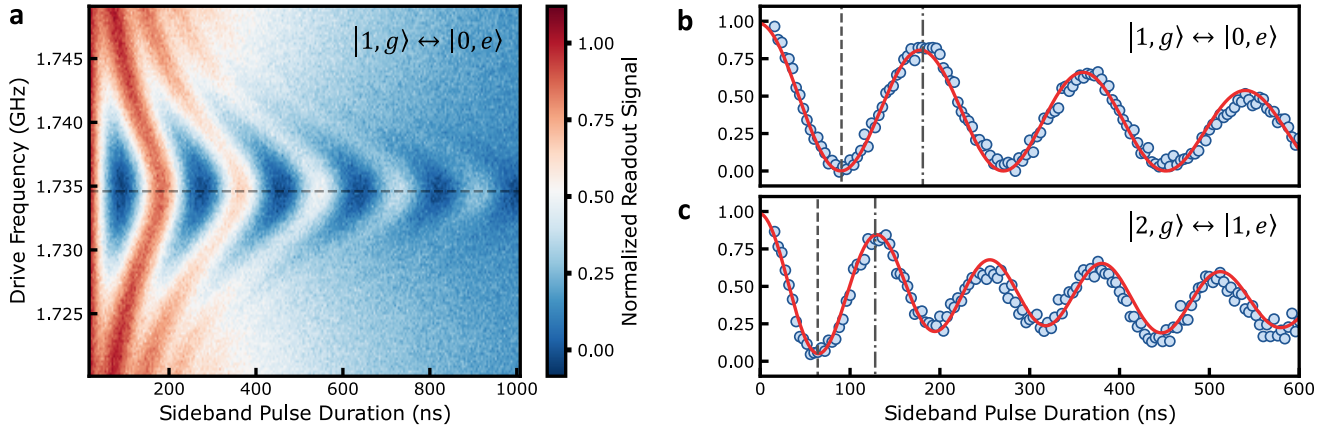


FIG. 4. Photon-pressure Jaynes-Cummings Ladder **a**, Photon-pressure Rabi chevrons with a single excitation in the system. The normalized output signal is proportional to the excited state probability of the qubit $P_{|e\rangle}$. **b**, Linecut of resonant Rabi oscillations for the $|1, g\rangle \leftrightarrow |0, e\rangle$ transition. A Rabi frequency $g = 2\pi \times 2.76$ MHz was used in the numerical simulation. The dashed lines indicate the photon-pressure pi-pulse duration $t_\pi = 90.5$ ns. The dotted dashed lines indicate the Rabi oscillation period, and the solid red line is a numerical simulation of the Rabi oscillations. **c**, Linecut of resonant Rabi oscillations for the $|2, g\rangle \leftrightarrow |1, e\rangle$ transition. An increased Rabi frequency $g_2 \approx \sqrt{2}g$ is observed. The dashed lines indicate the predicted second manifold photon-pressure pi-pulse duration $t_{\pi,2} = 90.5/\sqrt{2}$ ns. The dotted dashed lines indicate the Rabi oscillation period, and the solid red line is a numerical simulation of the Rabi oscillations.

tract the coupling rate $g/2\pi = 2.76 \pm 0.03$ MHz,²² resulting in a photon-pressure π -pulse duration of ~ 91 ns; see Fig. 4(b). This is in excellent agreement with the measured normal mode splitting at nominally the same sideband power, $g/2\pi = 2.81 \pm 0.08$ MHz. Finally, we observe transitions to higher excited manifolds of the Jaynes-Cummings ladder by preparing the linear oscillator in the Fock state $|1\rangle$ using a photon-pressure π -pulse and measuring the Rabi oscillations. We observe a Rabi frequency with a value $g_2 \approx \sqrt{2}g$, as predicted by the Jaynes-Cummings model²²; see Fig. 4(c).

DISCUSSION

This work presents a novel superconducting qubit coupled to a linear microwave resonator via a parametric photon-pressure interaction. The interaction was confirmed by performing normal-mode spectroscopy of the hybrid modes induced via a strong sideband drive and observing coherent Rabi oscillations. The value of the single-photon coupling rate was determined by calibrating the sideband drive using the AC-Stark shift. Our device is well within the single-photon strong coupling limit, a regime attained here for the first time to the best of our knowledge.

The photon-pressure qubit design provides a novel platform for testing theories demanding single-photon strong coupling, such as dissipative Schrödinger cat state generation within the microwave resonator²⁰. Moreover, the large critical photon number, $n_{\text{crit}} \approx 125\,000$, and the ability to dynamically modulate the coupling should allow for future integration with optomechanics experiments. In such an experiment, the cat state generated within the linear resonator can be swapped into a mechanical oscillator using a strong optomechanical side-

band pulse, generating a macroscopic superposition allowing for exotic tests of gravitational decoherence³³. Such a swap to the mechanical resonator would *not* be possible using conventional Jaynes-Cummings coupling due to the large driving requirements on the linear microwave cavity.

Moreover, this qubit may also be used for novel on-chip quantum optics; for example, at the top sweet-spot to first order, the linear coupling should be suppressed, *i.e.* $g_0 \approx 0$; however, there will remain quadratic coupling of the form $\hat{\mathcal{H}}_q/\hbar = g_q \hat{a}^\dagger \hat{a} (\hat{b} + \hat{b}^\dagger)^2$. Quadratic coupling has been long sought and was an initial driving force for the membrane in the middle experiments⁴². By eliminating linear coupling, the quadratic coupling may allow quantum non-demolition measurement of the photon number within the linear resonator⁴³, enabling an on-chip cQED measurement of stochastic photon jumps as they decay from the linear resonator^{44,45}.

Beyond interesting non-linear experiments, the qubit can be explored as a novel architecture for quantum information systems. Multiple qubits could be coupled to a single bus resonator, and by applying appropriate sideband pulses, it may be possible to implement photon-pressure mediated qubit-qubit gates. Having all qubits connected via the photon-pressure interaction to a single bus resonator would allow a fully superconducting implementation of efficient quantum computation architectures currently studied using ion-traps⁴⁶. Such a demonstration will open the door for future exploration of photon-pressure as a route for constructing highly scalable quantum information processing hardware²⁸.

ACKNOWLEDGMENTS

The authors thank V.A.S.V Bittencourt for helpful discussions and Enrique Sahagun for the device rendering⁴⁷. C.A.P. acknowledges the support of the Natural Sciences and Engineering Research Council of Canada (NSERC), and R.C.D acknowledges support from the Netherlands Organisation for Scientific Research (NWO/OCW) as part of the Frontiers of Nanoscience program.

This publication is part of the project ‘Superconducting Electromechanics: Massive superpositions for exploring quantum mechanics and general relativity.’ project number VI.C.212.087 of the research programme VICI round 2021, financed by the Dutch Research Council (NWO).

Authors contributions: C.A.P. performed theoretical modelling, performed data analysis, designed the qubit, performed daily supervision of measurements and coordination of the team, wrote the first draft of the manuscript with input from all authors, and incorporated feedback from authors into the final manuscript. R.C.D. designed and simulated the full device layout, developed the fabrication recipe and fabricated the device, performed spectroscopic measurements, contributed to data analysis, and contributed to figure design. S.D. contributed to the verification of theoretical models. S.D. and E.S. performed time-domain qubit measurements and analysis of those measurements. G.A.S. was responsible for conceiving the experiment, overall supervision of the project, and the acquisition of funding for the project. All authors contributed to the formulation of the storyline of the manuscript and the composition of the figures.

Competing interests: The authors declare no competing interests.

Data and materials availability: All data, analysis code, and measurement software are available in the manuscript or the supplementary information or are available at Zenodo.

¹M. Aspelmeyer, T. J. Kippenberg, and F. Marquardt, "Cavity optomechanics," *Rev. Mod. Phys.* **86**, 1391–1452 (2014).

²X. Zhang, C.-L. Zou, L. Jiang, and H. X. Tang, "Cavity magnomechanics," *Science Advances* **2**, e1501286 (2016).

³C. A. Potts, E. Varga, V. A. S. V. Bittencourt, S. Viola-Kusminskiy, and J. P. Davis, "Dynamical Backaction Magnomechanics," *Phys. Rev. X* **11**, 031053 (2021).

⁴R.-C. Shen, J. Li, Z.-Y. Fan, Y.-P. Wang, and J. Q. You, "Mechanical Bistability in Kerr-modified Cavity Magnomechanics," *Phys. Rev. Lett.* **129**, 123601 (2022).

⁵C. A. Potts, Y. Huang, V. A. S. V. Bittencourt, S. Viola-Kusminskiy, and J. P. Davis, "Dynamical backaction evading magnomechanics," *Physical Review B* **107**, L140405 (2023).

⁶C. Eichler and J. R. Petta, "Realizing a Circuit Analog of an Optomechanical System with Longitudinally Coupled Superconducting Resonators," *Phys. Rev. Lett.* **120**, 227702 (2018).

⁷D. Bothner, I. C. Rodrigues, and G. A. Steele, "Photon-pressure strong coupling between two superconducting circuits," *Nature Physics* **17**, 85–91 (2021).

⁸I. C. Rodrigues, D. Bothner, and G. A. Steele, "Cooling photon-pressure circuits into the quantum regime," *Science Advances* **7**, eabg6653 (2021).

⁹I. C. Rodrigues, G. A. Steele, and D. Bothner, "Parametrically enhanced interactions and nonreciprocal bath dynamics in a photon-pressure Kerr amplifier," *Science Advances* **8**, eabq1690 (2022).

¹⁰I. C. Rodrigues, G. A. Steele, and D. Bothner, "Photon-Pressure with a Negative Mass Microwave Mode," arXiv preprint arXiv:2212.07461 (2022).

¹¹D. Leibfried, R. Blatt, C. Monroe, and D. Wineland, "Quantum dynamics of single trapped ions," *Reviews of Modern Physics* **75**, 281 (2003).

¹²Y. Seis, T. Capelle, E. Langman, S. Saarinen, E. Planz, and A. Schliesser, "Ground state cooling of an ultracoherent electromechanical system," *Nature communications* **13**, 1507 (2022).

¹³J. D. Teufel, T. Donner, D. Li, J. W. Harlow, M. Allman, K. Cicak, A. J. Sirois, J. D. Whittaker, K. W. Lehnert, and R. W. Simmonds, "Sideband cooling of micromechanical motion to the quantum ground state," *Nature* **475**, 359–363 (2011).

¹⁴A. Noguchi, R. Yamazaki, M. Ataka, H. Fujita, Y. Tabuchi, T. Ishikawa, K. Usami, and Y. Nakamura, "Ground state cooling of a quantum electromechanical system with a silicon nitride membrane in a 3D loop-gap cavity," *New Journal of Physics* **18**, 103036 (2016).

¹⁵S. Kotler, G. A. Peterson, E. Shojaee, F. Lecocq, K. Cicak, A. Kwiatkowski, S. Geller, S. Glancy, E. Knill, R. W. Simmonds, *et al.*, "Direct observation of deterministic macroscopic entanglement," *Science* **372**, 622–625 (2021).

¹⁶R. W. Andrews, R. W. Peterson, T. P. Purdy, K. Cicak, R. W. Simmonds, C. A. Regal, and K. W. Lehnert, "Bidirectional and efficient conversion between microwave and optical light," *Nature physics* **10**, 321–326 (2014).

¹⁷W. Jiang, C. J. Sarabalis, Y. D. Dahmani, R. N. Patel, F. M. Mayor, T. P. McKenna, R. Van Laer, and A. H. Safavi-Naeini, "Efficient bidirectional piezo-optomechanical transduction between microwave and optical frequency," *Nature communications* **11**, 1166 (2020).

¹⁸J. B. Hertzberg, T. Rocheleau, T. Ndukum, M. Savva, A. A. Clerk, and K. C. Schwab, "Back-action-evading measurements of nanomechanical motion," *Nature Physics* **6**, 213–217 (2010).

¹⁹F. Lecocq, J. B. Clark, R. W. Simmonds, J. Aumentado, and J. D. Teufel, "Quantum Nondemolition Measurement of a Nonclassical State of a Massive Object," *Phys. Rev. X* **5**, 041037 (2015).

²⁰B. D. Hauer, J. Combes, and J. D. Teufel, "Nonlinear Sideband Cooling to a Cat State of Motion," *Phys. Rev. Lett.* **130**, 213604 (2023).

²¹A. Blais, A. L. Grimsom, S. M. Girvin, and A. Wallraff, "Circuit quantum electrodynamics," *Reviews of Modern Physics* **93**, 025005 (2021).

²²M. Hofheinz, E. M. Weig, M. Ansmann, R. C. Bialczak, E. Lucero, M. Neeley, A. O'connell, H. Wang, J. M. Martinis, and A. N. Cleland, "Generation of Fock states in a superconducting quantum circuit," *Nature* **454**, 310–314 (2008).

²³M. Hofheinz, H. Wang, M. Ansmann, R. C. Bialczak, E. Lucero, M. Neeley, A. O'connell, D. Sank, J. Wenner, J. M. Martinis, *et al.*, "Synthesizing arbitrary quantum states in a superconducting resonator," *Nature* **459**, 546–549 (2009).

²⁴F. Yan, P. Krantz, Y. Sung, M. Kjaergaard, D. L. Campbell, T. P. Orlando, S. Gustavsson, and W. D. Oliver, "Tunable Coupling Scheme for Implementing High-Fidelity Two-Qubit Gates," *Phys. Rev. Appl.* **10**, 054062 (2018).

²⁵R. C. Bialczak, M. Ansmann, M. Hofheinz, M. Lenander, E. Lucero, M. Neeley, A. D. O'Connell, D. Sank, H. Wang, M. Weides, J. Wenner, T. Yamamoto, A. N. Cleland, and J. M. Martinis, "Fast Tunable Coupler for Superconducting Qubits," *Phys. Rev. Lett.* **106**, 060501 (2011).

²⁶Z. Ni, S. Li, L. Zhang, J. Chu, J. Niu, T. Yan, X. Deng, L. Hu, J. Li, Y. Zhong, S. Liu, F. Yan, Y. Xu, and D. Yu, "Scalable Method for Eliminating Residual ZZ Interaction between Superconducting Qubits," *Phys. Rev. Lett.* **129**, 040502 (2022).

²⁷B.-m. Ann, W. Kessels, and G. A. Steele, "Sideband transitions in a two-mode Josephson circuit driven beyond the rotating-wave approximation," *Phys. Rev. Res.* **3**, 033004 (2021).

²⁸P.-M. Billangeon, J. S. Tsai, and Y. Nakamura, "Circuit-QED-based scalable architectures for quantum information processing with superconducting qubits," *Phys. Rev. B* **91**, 094517 (2015).

²⁹P. Panteleev and G. Kalachev, "Quantum LDPC codes with almost linear minimum distance," *IEEE Transactions on Information Theory* **68**, 213–229 (2021).

³⁰A. Fedorov, L. Steffen, M. Baur, M. P. da Silva, and A. Wallraff, "Implementation of a Toffoli gate with superconducting circuits," *Nature* **481**, 170–172 (2012).

³¹A. Nunnenkamp, K. Børkje, and S. M. Girvin, "Single-photon optomechanics," *Physical review letters* **107**, 063602 (2011).

³²A. Nunnenkamp, K. Børkje, and S. M. Girvin, "Cooling in the single-photon strong-coupling regime of cavity optomechanics," *Physical Review A* **85**, 051803 (2012).

³³M. F. Gely and G. A. Steele, "Superconducting electro-mechanics to test Diosi-Penrose effects of general relativity in massive superpositions," *AVS Quantum Science* **3**, 035601 (2021).

³⁴P. Krantz, M. Kjaergaard, F. Yan, T. P. Orlando, S. Gustavsson, and W. D. Oliver, "A quantum engineer's guide to superconducting qubits," *Applied Physics Reviews* **6**, 021318 (2019).

³⁵M. Boissonneault, J. M. Gambetta, and A. Blais, "Dispersive regime of circuit QED: Photon-dependent qubit dephasing and relaxation rates," *Phys. Rev. A* **79**, 013819 (2009).

³⁶Qiskit contributors, "Qiskit: An Open-source Framework for Quantum Computing," (2023).

³⁷A. Wallraff, D. Schuster, A. Blais, J. Gambetta, J. Schreier, L. Frunzio, M. Devoret, S. Girvin, and R. Schoelkopf, "Sideband transitions and two-tone spectroscopy of a superconducting qubit strongly coupled to an on-chip cavity," *Physical Review Letters* **99**, 050501 (2007).

³⁸C. Gardiner and P. Zoller, *Quantum noise: a handbook of Markovian and non-Markovian quantum stochastic methods with applications to quantum optics* (Springer Science & Business Media, 2004).

³⁹J. M. Fink, M. Göppl, M. Baur, R. Bianchetti, P. J. Leek, A. Blais, and A. Wallraff, "Climbing the Jaynes–Cummings ladder and observing its nonlinearity in a cavity QED system," *Nature* **454**, 315–318 (2008).

⁴⁰M. L. Gorodetsky, A. Schliesser, G. Anetsberger, S. Deleglise, and T. J. Kippenberg, "Determination of the vacuum optomechanical coupling rate using frequency noise calibration," *Opt. Express* **18**, 23236–23246 (2010).

⁴¹A. J. R. MacDonald, B. D. Hauer, X. Rojas, P. H. Kim, G. G. Popovich, and J. P. Davis, "Optomechanics and thermometry of cryogenic silica microresonators," *Phys. Rev. A* **93**, 013836 (2016).

⁴²A. Nunnenkamp, K. Børkje, J. G. E. Harris, and S. M. Girvin, “Cooling and squeezing via quadratic optomechanical coupling,” *Physical Review A* **82**, 021806 (2010).

⁴³B. D. Hauer, A. Metelmann, and J. P. Davis, “Phonon quantum nondemolition measurements in nonlinearly coupled optomechanical cavities,” *Physical Review A* **98**, 043804 (2018).

⁴⁴C. Guerlin, J. Bernu, S. Deleglise, C. Sayrin, S. Gleyzes, S. Kuhr, M. Brune, J.-M. Raimond, and S. Haroche, “Progressive field-state collapse and quantum non-demolition photon counting,” *Nature* **448**, 889–893 (2007).

⁴⁵S. Gleyzes, S. Kuhr, C. Guerlin, J. Bernu, S. Deleglise, U. Busk Hoff, M. Brune, J.-M. Raimond, and S. Haroche, “Quantum jumps of light recording the birth and death of a photon in a cavity,” *Nature* **446**, 297–300 (2007).

⁴⁶K. Wright, K. M. Beck, S. Debnath, J. Amini, Y. Nam, N. Grzesiak, J.-S. Chen, N. Pisenti, M. Chmielewski, C. Collins, *et al.*, “Benchmarking an 11-qubit quantum computer,” *Nature communications* **10**, 5464 (2019).

⁴⁷“Scixel,” <https://scixel.es/>, accessed: 2023-09-28.

⁴⁸D. J. Thoen, B. G. C. Bos, E. Haalebos, T. Klapwijk, J. Baselmans, and A. Endo, “Superconducting NbTiN Thin Films With Highly Uniform Properties Over a 100 mm Wafer,” *IEEE Transactions on Applied Superconductivity* **27**, 1–5 (2016).

⁴⁹R. Igreja and C. J. Dias, “Analytical evaluation of the interdigital electrodes capacitance for a multi-layered structure,” *Sensors and Actuators A: Physical* **112**, 291–301 (2004).

⁵⁰J. R. Johansson, P. D. Nation, and F. Nori, “Qutip: An open-source python framework for the dynamics of open quantum systems,” *Computer Physics Communications* **183**, 1760–1772 (2012).

⁵¹T. Abad, J. Fernández-Pendás, A. Frisk Kockum, and G. Johansson, “Universal fidelity reduction of quantum operations from weak dissipation,” *Physical Review Letters* **129**, 150504 (2022).

⁵²D. Zoepfl, M. L. Juan, N. Diaz-Naufal, C. M. F. Schneider, L. F. Deeg, A. Sharafiev, A. Metelmann, and G. Kirchmair, “Kerr Enhanced Backaction Cooling in Magnetomechanics,” *Phys. Rev. Lett.* **130**, 033601 (2023).

⁵³A. Reiserer and G. Rempe, “Cavity-based quantum networks with single atoms and optical photons,” *Reviews of Modern Physics* **87**, 1379 (2015)

Supplementary Information: Parametric Light-Matter Interaction in the Single-Photon Strong Coupling Limit

C.A. Potts, R.C. Dekker, S. Deve, E.W. Strijbis, G.A. Steele

Kavli Institute of Nanoscience, Delft University of Technology, PO Box 5046, 2600 GA Delft, The Netherlands

I. MATERIALS AND METHODS

A. Device Fabrication

The device is fabricated on 10x10 mm 525 μm thick high-resistivity silicon chips with 200 nm of niobium-titanium nitride (NbTiN). The NbTiN is deposited by the Dutch Institute for Space Research (SRON) following the procedure described in Ref.⁴⁸. The bulk of the circuitry is fabricated by spinning a (positive) e-beam resist layer (AR-P 6200.18, 4000 rpm) and patterning the CPW, linear resonator, qubit islands and feedlines using electron-beam lithography. After development (Pentylacetate, O-xylene, IPA) and a post-exposure bake, the NbTiN is removed using an SF₆ reactive ion etching step, followed by an in-situ oxygen plasma descum. After stripping the resist, the Josephson junctions are fabricated by depositing an MMA/PMMA resist bi-layer and patterning the junctions using electron-beam lithography. The resist is developed using cold H₂O:IPA (1:3) and IPA. The chip is dipped in a buffered oxide etchant (BOE) for 1 min prior to loading into the Plassys deposition system. The junctions are evaporated using a double-angle deposition technique, forming a pair of Manhattan-style Josephson junctions. After liftoff in NMP and wire bonding, the chips are loaded into the dilution refrigerator.

B. Measurement Setup

All measurements were performed on the base plate of a dilution refrigerator operating at a base temperature $T \sim 15$ mK. A complete schematic of the wiring within the fridge is shown in Fig. S1. The $\lambda/2$ CPW readout resonator is connected to its own feedline via a cryogenic circulator and measured in reflection. The linear resonator is coupled in a notch-type geometry and measured in transmission using a different output line. Both output lines are passed through a pair of low-temperature isolators and via superconducting coaxial cables to a pair of HEMT amplifiers and additional amplification at room temperature. The input lines connecting to the $\lambda/2$ CPW resonator, the qubit drive line, and the input line of the linear resonator all have 59 dB of cryogenic attenuation, with additional room-temperature attenuation. The device is mounted in a light-tight copper box on a copper bracket within a superconducting aluminum and Mu-metal magnetic shield. An external superconducting coil magnet is mounted underneath the copper sample box and inside the magnetic shielding. Spectroscopic measurements were performed using a four-port Keysight PNA for both the qubit and linear resonator, and the time domain measurements were performed using a Quantum Machines OPX, Octave and Rohde & Schwarz SGS100A vector microwave generator.

C. Zero-Point Current Fluctuations

The linear RF circuit consists of a set of interdigitated capacitors (IDC) with a thin inductor wire; see Fig. S2. The capacitance of the IDC can be estimated analytically following Ref.⁴⁹,

$$C_{\text{IDC}} = (N - 3) \frac{C_1}{2} + 2 \frac{C_1 C_2}{C_1 + C_2} \quad (\text{S1})$$

where

$$C_i = 2\epsilon_0 \epsilon_{\text{eff}} l \frac{K(k_i)}{K(k'_i)}, \quad i = 1, 2. \quad (\text{S2})$$

Here, $K(k_i)$ are the elliptic integrals of the first kind, l is the length of the IDC fingers, $\epsilon_{\text{eff}} = (\epsilon_r + 1)/2$ is the effective permittivity where the permittivity of silicon is $\epsilon_r = 11.8$, N is the total number of fingers and

$$k_1 = \sin \left(\frac{\pi}{2} \frac{a}{a + b} \right), \quad (\text{S3})$$

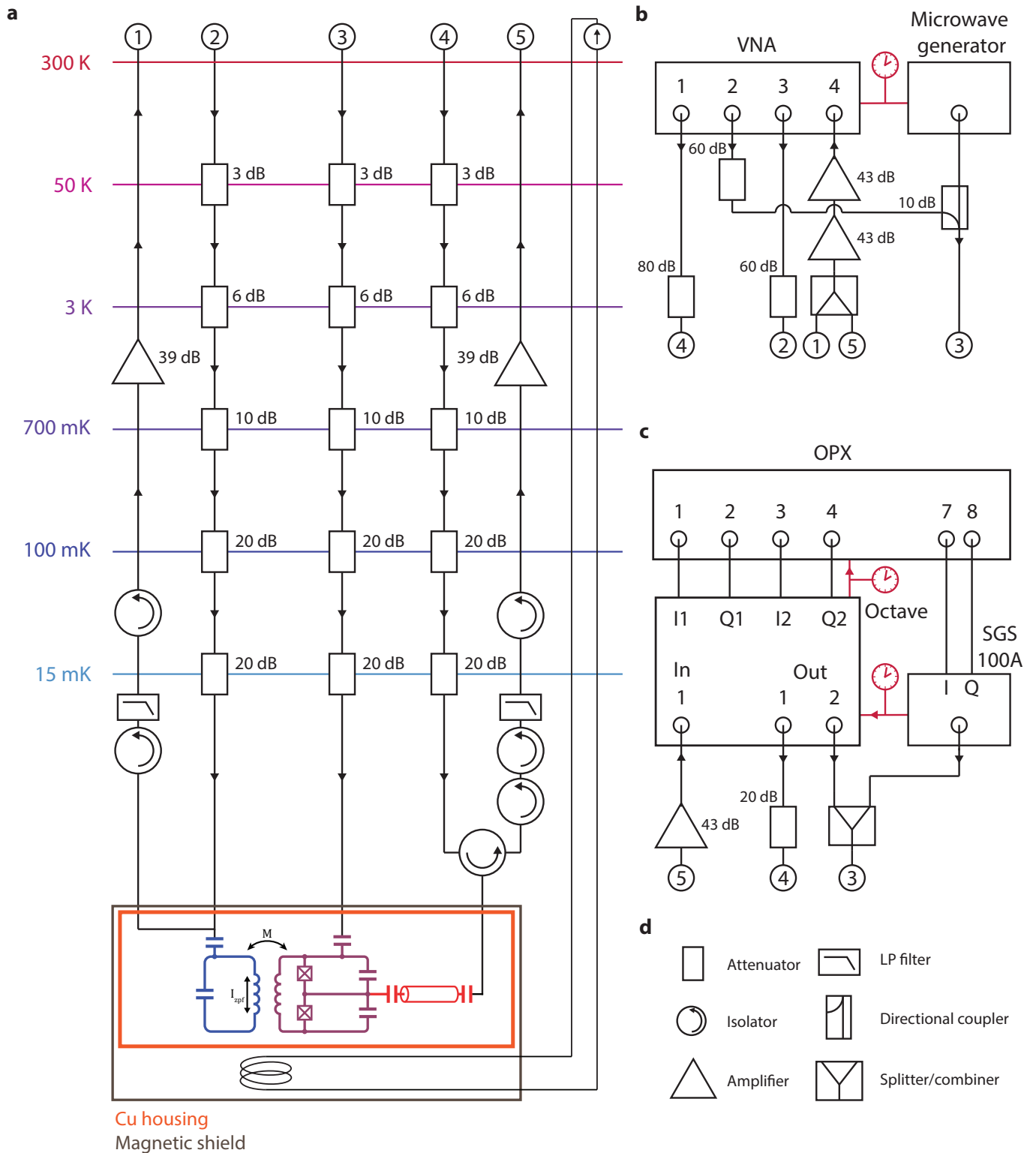


FIG. S1. **Schematic of the measurement setup.** **a**, Wiring diagram inside the dilution refrigerator. **b**, Room temperature setup for VNA measurements. **c**, Setup for time domain measurements. **d**, Overview of components.

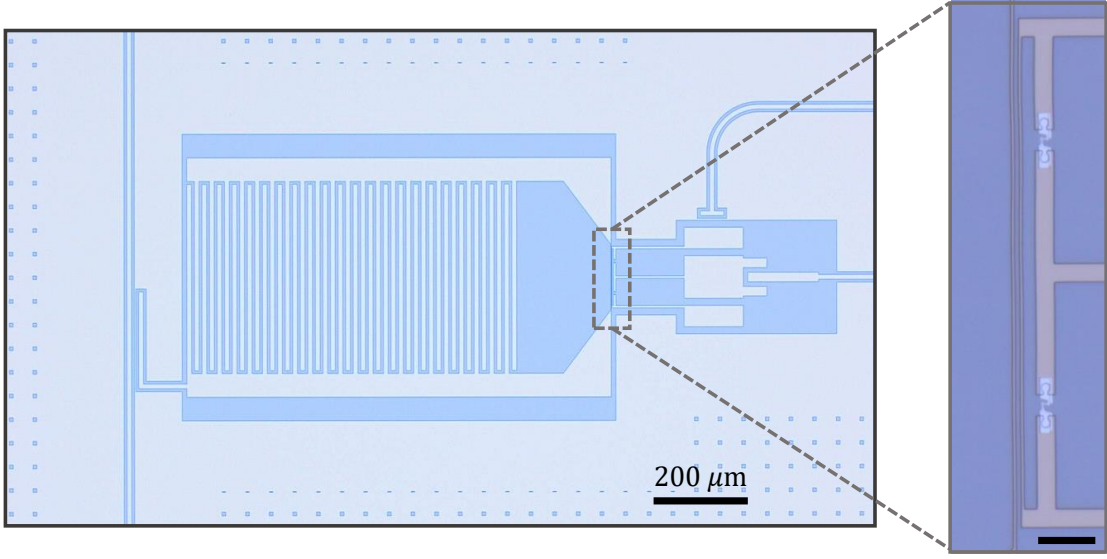


FIG. S2. **Photon-pressure circuit.** **a**, Optical micrograph image of the qubit. The scale bar on the zoom is 15 μm .

$$k_2 = 2 \frac{\sqrt{a(a+b)}}{2a+b}, \quad (\text{S4})$$

$$k'_i = \sqrt{1 - k_i^2}, \quad (\text{S5})$$

where, a is the finger width, and b is the gap between fingers. The fabricated linear resonator has $N = 44$, $a = 10\mu\text{m}$, $b = 6\mu\text{m}$, and $l = 400\mu\text{m}$. Therefore, Eq. S2 estimates the capacitance of the linear circuit as $C_{\text{IDC}} = 1.26 \text{ pF}$, which is in excellent agreement with the Ansys capacitance simulation calculating a total capacitance of $C_b = 1.29 \text{ pF}$, suggesting there is little stray capacitance from the remainder of the circuit. The measured resonance frequency of the circuit is $\omega_b = 2\pi \times 4.347 \text{ GHz}$. Assuming the IDC capacitance is the only capacitance in the circuit, we can determine the circuit inductance by

$$\omega_b = \frac{1}{\sqrt{L_b C_b}}. \quad (\text{S6})$$

giving a total inductance of $L_b = 1.06 \text{ nH}$. Therefore, the current zero-point fluctuations through the inductor of the linear circuit are given by

$$I_{\text{zpf}} = \sqrt{\frac{\hbar \omega_b}{2L_b}} \quad (\text{S7})$$

with the values calculated above, the zero-point current $I_{\text{zpf}} \approx 36.8 \text{ nA}$.

D. Parasitic Coupling

As discussed in the main text, the qubit was designed to minimize dipole coupling between the qubit and the linear resonator. The linear interaction of the form $\mathcal{H}_{\text{JC}}/\hbar = g_{ab}(\hat{\sigma}_+ \hat{b} + \hat{\sigma}_- \hat{b}^\dagger)$ results in the hybridization of the qubit with

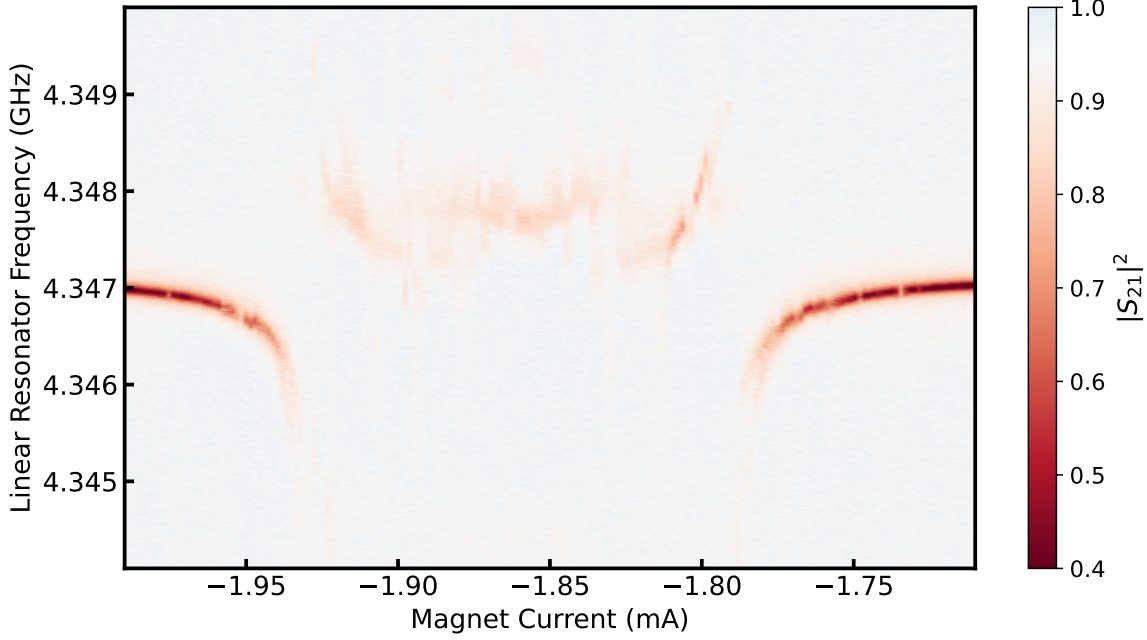


FIG. S3. **Avoided level crossing between qubit and linear resonator** a, Measured transmission spectra $|S_{21}|^2$ of the linear circuit as the qubit's frequency is swept through the linear resonator's frequency. Two avoided crosses are observed as the qubit tunes down to the bottom sweet spot. We can extract the linear coupling coefficient g_{ab} between the linear circuit and the qubit from the avoided crossing. The additional features at -1.85 mA are attributed to a higher order mode of the qubit being tuned into resonance with the linear resonator.

the linear resonator. Even in the dispersive regime, where $\Delta \gg g_{ab}$, the weak hybridization results in a critical photon number, $n_{\text{crit}} = \Delta^2/(4g_{ab}^2)$, in which the dispersive approximation breaks down²¹. Here, $\hat{\sigma}_{\pm}$ are the qubit raising and lowering operators, $\hat{b}^{(\dagger)}$ are the linear circuit annihilation (creation) operators and $\Delta = |\omega_q - \omega_b|$ is the qubit detuning from the linear resonator.

Flux tuning the qubit to be approximately resonant with the linear resonator results in an avoided level crossing, as shown in Fig. S3. The dipole coupling is given by the frequency difference between the upper and lower normal modes when the qubit and linear circuit are resonant. We extract a dipole coupling rate of $g_{ab} \approx 2\pi \times 2.5$ MHz, several orders of magnitude smaller than current state-of-the-art circuit quantum electrodynamics devices²¹. The qubit operational point used in this work was detuned from the linear circuit by $\Delta = 1.75$ GHz; therefore, we estimate a critical photon number within the linear circuit of $n_{\text{crit}} \approx 125\,000$.

E. Photon-Pressure Coupling Estimation

The mutual inductive coupling between the inductor wire of the linear circuit and the SQUID loop of the qubit quantifies the coupling between the linear circuit and the qubit. As shown in Fig. S2, the SQUID loop of the qubit has a designed length $l = 120\mu\text{m}$ and width $w = 3\mu\text{m}$, giving a nominal SQUID area of $360\mu\text{m}^2$; however, the final dimensions were slightly larger due to over-etching. The $1.0\mu\text{m}$ wide inductor wire passes $\sim 1.0\mu\text{m}$ from the SQUID loop, with measured geometric distances $d_1 \approx 1.8\mu\text{m}$ and $d_2 \approx 5.3\mu\text{m}$ are the smallest and largest distance between the inductor and the SQUID loop, respectively; see Fig. S2. The mutual inductance can be calculated by integrating the magnetic flux generated by the inductor wire through the SQUID loop and is given by

$$M = \frac{\mu_0 l}{2\pi} \ln \left(\frac{d_2}{d_1} \right). \quad (\text{S8})$$

Using this approximation, we find a mutual inductance $M \approx 25.9$ pH. Moreover, we can determine the zero-point fluctuations of the magnetic flux using the zero-point current giving $\Phi_{\text{zpf}} = MI_{\text{zpf}} \approx 461 \mu\Phi_0$ where we have written the zero-point magnetic-flux fluctuations in units of flux quanta $\Phi_0 = h/(2e)$.

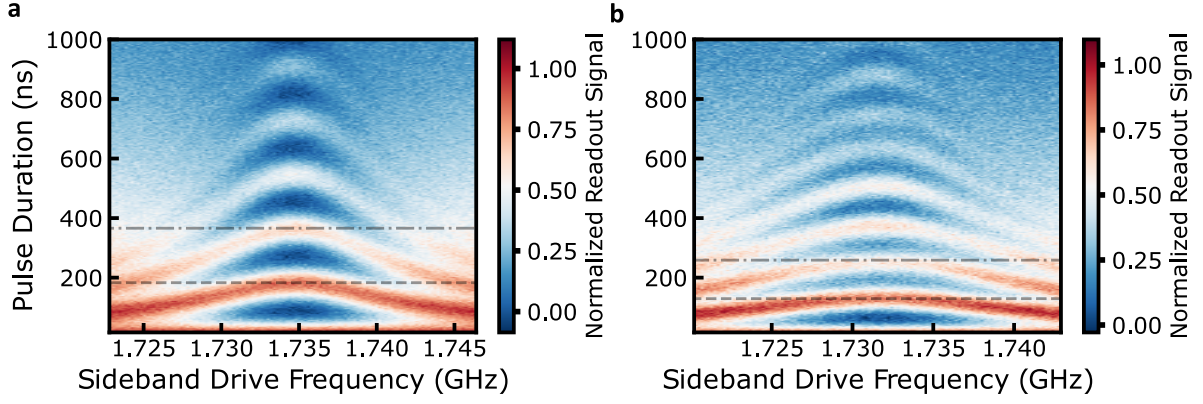


FIG. S4. **Photon-pressure Jaynes-Cummings Ladder** **a**, Photon-pressure Rabi chevrons with a single excitation in the system. A Rabi frequency $g = 2\pi \times 2.73$ MHz was measured. **b**, Photon-pressure Rabi chevrons with two total excitations in the system. The linear resonator is prepared into the Fock state $|1\rangle$ using a photon-pressure π -pulse. Following the state preparation, the Rabi chevron was measured. An increased Rabi frequency $g_2 \approx \sqrt{2}g$. The dashed lines indicate the Rabi oscillation period, and the dotted dashed lines indicate two Rabi oscillation periods.

The single-photon coupling rate is defined as

$$g_0 = \frac{\partial \omega_q}{\partial \Phi} \Phi_{\text{zpf}}. \quad (\text{S9})$$

The single-photon coupling rate is the frequency shift of the qubit due to the zero-point fluctuations of the magnetic flux generated by the linear circuit. The frequency responsivity of the qubit can be determined by sweeping the external magnetic field at the operation frequency; we find $|\partial \omega_q / \partial \Phi| \approx 2\pi \times 26.0$ GHz/ Φ_0 . Therefore, at the operation point, we estimate a single-photon coupling rate of $g_0 \approx 2\pi \times 12.0$ MHz, which is in excellent agreement with the experimentally measured value.

F. Photon-Pressure Jaynes-Cummings

To confirm that the photon-pressure interaction is indeed described by the Jaynes-Cummings Hamiltonian, we compared the single and two-excitation Rabi frequencies. The single excitation Rabi frequency was measured as described in the main text. The data was fit using a numerical simulation described below, where we excite the qubit into the state $|1\rangle$ using a resonant π -pulse. To determine the two-excitation Rabi frequency, we first initialize the linear resonator into the Fock state $|1\rangle$ by performing a photon-pressure π -pulse. This was followed by a measurement of the Rabi chevron, shown in Fig. S4(b). We observe a clear increase in the Rabi frequency as predicted by the Jaynes-Cummings model; the Rabi frequency increases by a factor of approximately square root two. We use our numerical simulation to determine the Rabi frequency given by $g = 2\pi \times 2.76$ MHz, which is in good agreement with a fit of the line-cut to a decaying sinusoidal function giving a value $g = 2\pi \times 2.73$ MHz. We attribute any small discrepancy to the fidelity of our initial preparation of the linear resonator Fock state. Due to losses within the system, on average, the state of the linear resonator is likely a mixed state of $|0\rangle$ and $|1\rangle$, reducing the ensemble-averaged Rabi frequency measured here. However, this measurement does confirm that the photon-pressure interaction produces a Jaynes-Cummings ladder. With device optimization, this will be explored in future work.

G. Master Equation Simulation

To model the dynamics of the Jaynes-Cummings interaction, we simulate the system using the Lindblad Master equation using the Python package Qutip⁵⁰. The dynamics are governed by the equation given by,

$$\frac{\partial \rho}{\partial t} = -\frac{i}{\hbar} [\hat{\mathcal{H}}(t), \rho] + \kappa_b \mathcal{L}[\hat{b}]\rho + \gamma_1 \mathcal{L}[\hat{\sigma}_-]\rho, \quad (\text{S10})$$

where ρ is the system's density matrix, κ_b is the total decay rate of the linear microwave resonator, and γ_1 is the qubit relaxation rate. We do not consider dephasing here since single-shot projections on the z-axis are insensitive to

fast frequency fluctuations, and $T_{2\text{echo}}$ in our experiment is much greater than T_1 ⁵¹. The system Hamiltonian derived below is given by,

$$\hat{\mathcal{H}}(t)/\hbar = -\frac{\Delta_q}{2}\hat{\sigma}_z + \omega_b\hat{b}^\dagger\hat{b} + g(t)(\hat{\sigma}_+\hat{b} + \hat{\sigma}_-\hat{b}^\dagger) + \epsilon_d(t)(\hat{\sigma}_+e^{-i\Delta_q t} + \hat{\sigma}_-e^{i\Delta_q t}). \quad (\text{S11})$$

Here, $\Delta_q = \omega_d - \omega_q$ is the drive detuning, $g(t)$ is the time dependent coupling rate, and $\epsilon_d(t)$ is a time dependent resonant qubit drive. The system is initially prepared in its ground state, and the qubit is prepared with a sequence of resonant square wave π -pulses 24 ns in duration and photon-pressure π -swap pulses 91 ns in duration. The resultant time traces are plotted in Fig. 4 and show excellent agreement with the experimental results.

II. DEVICE CHARACTERIZATION

A. Linear Circuit Parameter Extraction

The linear microwave resonator is coupled to a transmission line in the ‘notch’ style geometry. Thus, the data is fitted to the transmission response function

$$S_{21}^{\text{notch}}(\omega) = 1 - \frac{\kappa_{\text{ext}}e^{i\theta}}{(\kappa_{\text{int}} + \kappa_{\text{ext}}) + 2i(\omega - \omega_b)}. \quad (\text{S12})$$

Here, θ accounts for any impedance mismatch, ω_b is the resonance frequency, and κ_{int} and κ_{ext} are the internal decay rate and the decay rate into the transmission line, respectively. The fit of the measured transmission spectrum is shown in Fig. S5. We extract the parameters $\omega_b = 2\pi \times 4.347$ GHz, $\kappa_{\text{int}} = 2\pi \times 28.0$ kHz, $\kappa_{\text{ext}} = 2\pi \times 88.6$ kHz, and $\kappa = 2\pi \times 116.6$ kHz.

B. Photon-Pressure Qubit Design

1. Qubit Characterization

The initial characterization of the qubit was done using two-tone spectroscopy. A weak pump tone was applied near the qubit frequency while simultaneously monitoring the frequency of the readout CPW. This technique allows the determination of the qubit frequency and the anharmonicity of the qubit. By sweeping the external magnetic field, we are able to map out the qubit flux arc. We found a sweet spot frequency $\omega_q = 2\pi \times 10.2$ GHz and could tune the qubit frequency below 500 MHz. Next, with the qubit at its operational point, by increasing the qubit pump tone, we

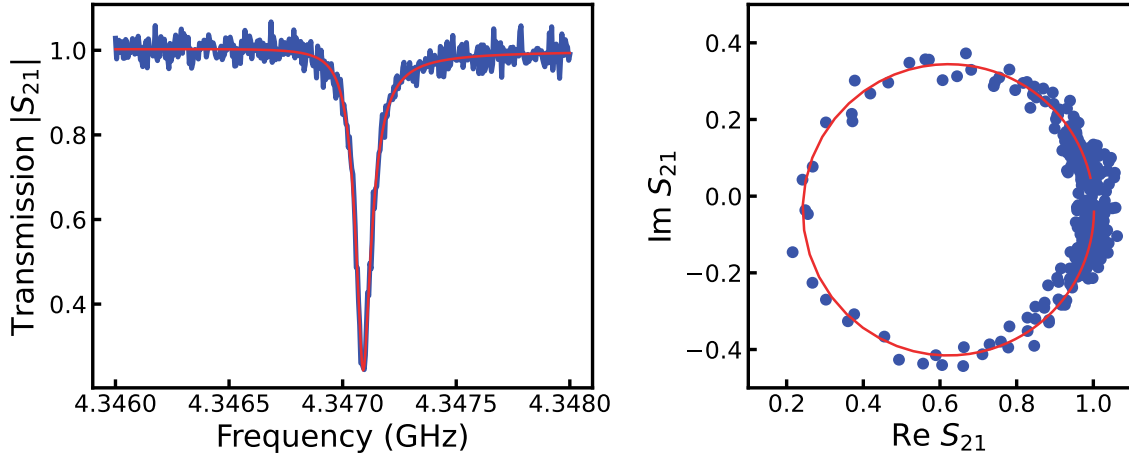


FIG. S5. **The linear circuit response.** **a**, The magnitude of the transmission response $|S_{21}|$ of the linear resonator. **b**, The complex transmission data S_{21} near the resonance frequency of the linear resonator. In both plots, the circles are data; the line is a fit. The data plotted here has had its background subtracted.

are able to measure the anharmonicity by driving the $|1\rangle \rightarrow |2\rangle$ transition. We find an anharmonicity $\alpha = -2\pi \times 388$ MHz.

Next, the qubit was characterized by performing time domain measurements of its decay characteristics. At the operational point, the qubit has a $T_1 = 664$ ns and a $T_2^* = 235$ ns. These values are not state-of-the-art; however, they are not a result of the photon-pressure geometry since standard Xmon-style qubits fabricated using the same process show similar values for the characteristic decay rates. We have identified our most likely limiting factor to be our SF_6 etch step damaging the silicon surface prior to our junction deposition. This is currently a work in progress, and we aim to improve our coherence time with future devices. Secondly, we expect flux noise to limit our T_2^* ; this can be improved in future experiments by reducing the SQUID area and optimizing the mutual inductance to maintain a large g_0 . The current SQUID loop has an area $\sim 360\mu\text{m}^2$, likely resulting in large amounts of flux noise. The SQUID loop size can be reduced with device optimization, reducing flux noise.

III. PHOTON-PRESSURE THEORY

A. Quantization of Superconducting Qubit

As defined in Ref.³⁴, the Hamiltonian describing an LC oscillator is given by

$$\hat{\mathcal{H}} = 4E_C\hat{n}^2 + \frac{1}{2}E_L\hat{\phi}^2. \quad (\text{S13})$$

Here, $E_C = e^2/(2C)$, is the charging energy required to add each electron from the Cooper-pair to the island and $E_L = (\Phi_0/2\pi)^2/L$ is the inductive energy, where $\Phi_0 = h/(2e)$ is the magnetic flux quantum. The operator $\hat{n} = \hat{Q}/2e$ is the excess number of Cooper pairs on the island, and $\hat{\phi}$ is the gauge invariant phase across the inductor. Note that these form a pair of canonically conjugate variables $[\hat{\phi}, \hat{n}] = i$.

We can recast this Hamiltonian in the form,

$$\hat{\mathcal{H}} = \hbar\omega_q(\hat{a}^\dagger\hat{a} + 1/2), \quad (\text{S14})$$

where $\hat{a}(\hat{a}^\dagger)$ is the annihilation (creation) operator of a single excitation of the LC oscillator. The resonance frequency is defined as $\omega_q = \sqrt{8E_C E_L}/\hbar$ in anticipation of this circuit representing the transmon qubit. The charge and flux operators can be written in the form $\hat{n} = in_{\text{zpf}}(\hat{a} - \hat{a}^\dagger)$ and $\hat{\phi} = \phi_{\text{zpf}}(\hat{a} + \hat{a}^\dagger)$, where $n_{\text{zpf}} = (E_L/(32E_C))^{1/4}$ and $\phi_{\text{zpf}} = (2E_C/E_L)^{1/4}$.

Replacing the inductor with a Josephson junction results in the modified Hamiltonian of the form,

$$\hat{\mathcal{H}} = 4E_C\hat{n}^2 - E_J \cos(\hat{\phi}), \quad (\text{S15})$$

where $E_C = e^2/(2C_\Sigma)$, $C_\Sigma = C_s + C_J$ is the total capacitance, including the shunt capacitance and the self-capacitance of the Josephson junction, $E_J = I_c\Phi_0/2\pi$ is the Josephson energy, where I_c is the critical current of the junction. In the transmon limit (i.e. $E_J \gg E_C$), the fluctuations of $\hat{\phi}$ are small; therefore, we can expand the potential term, giving

$$E_J \cos(\hat{\phi}) = \frac{1}{2}E_J\hat{\phi}^2 - \frac{1}{24}E_J\hat{\phi}^4 + \mathcal{O}(\hat{\phi}^6). \quad (\text{S16})$$

The second term results in an anharmonic potential, with an anharmonicity given by $\alpha = \omega_q^{1 \rightarrow 2} - \omega_q^{0 \rightarrow 1}$. For a transmon qubit $\alpha = -E_C$, it is typically 100-300 MHz.

Keeping terms up to fourth order in creation and annihilation operators, the Hamiltonian can be written in the form,

$$\hat{\mathcal{H}}/\hbar = \omega_q\hat{a}^\dagger\hat{a} + \frac{\alpha}{2}\hat{a}^\dagger\hat{a}^\dagger\hat{a}\hat{a}, \quad (\text{S17})$$

which is the Hamiltonian for a Kerr oscillator. Rather than a single Josephson junction, a pair of junctions are used as a SQUID loop to provide flux tunability to the transmon qubit. The effective Hamiltonian of such a flux-tunable transmon is given by

$$\hat{\mathcal{H}} = 4E_C\hat{n}^2 - 2E_J|\cos(\varphi_e)|\cos\hat{\phi}. \quad (\text{S18})$$

Here φ_e is the externally applied magnetic flux. We can define an effective Josephson energy $\tilde{E}_J(\varphi_e) = 2E_J|\cos(\varphi_e)|$.

B. Photon-Pressure Hamiltonian

Considering the linear resonator and the coherent drive tones, the total Hamiltonian of the photon-pressure device is

$$\hat{\mathcal{H}} = 4E_C \hat{n}^2 - \tilde{E}_J(\varphi_e) \cos \hat{\phi} + \hbar \omega_b \hat{b}^\dagger \hat{b} + \hat{\mathcal{H}}_d. \quad (\text{S19})$$

Here, \hat{b} (\hat{b}^\dagger) are the annihilation (creation) operators for the linear resonator. During operation, the external flux bias is fixed at a single value, and due to the mutual inductive coupling between the linear circuit and the SQUID loop, the external flux is modulated by the linear resonator. We can, therefore, write the Josephson energy in the form

$$\tilde{E}_J(\varphi_e) = \bar{E}_J + \frac{dE_J}{d\varphi_e} \frac{d\varphi_e}{dI} I_{zpf}(\hat{b} + \hat{b}^\dagger). \quad (\text{S20})$$

Here, \bar{E}_J is the Josephson energy at the flux-bias point, $I_{zpf} = \sqrt{\hbar \omega_b / 2L_b}$, where L_b is the inductance of the linear resonator. We can simplify this equation by defining a coupling constant in the form

$$\hbar \tilde{g}_0 = \frac{dE_J}{d\varphi_e} \frac{d\varphi_e}{dI} I_{zpf}. \quad (\text{S21})$$

Therefore, the Hamiltonian can be written as,

$$\hat{\mathcal{H}} = 4E_C \hat{n}^2 - \bar{E}_J \cos \hat{\phi} - \hbar \tilde{g}_0 \cos \hat{\phi}(\hat{b} + \hat{b}^\dagger) + \hbar \omega_b \hat{b}^\dagger \hat{b} + \hat{\mathcal{H}}_d. \quad (\text{S22})$$

At this stage, we can expand the cosine of the gauge invariant flux using Eq. S16, giving

$$\hat{\mathcal{H}} = 4E_C \hat{n}^2 + \bar{E}_J \left(\frac{1}{2} \hat{\phi}^2 - \frac{1}{24} \hat{\phi}^4 \right) + \hbar \tilde{g}_0 \frac{1}{2} \hat{\phi}^2 (\hat{b} + \hat{b}^\dagger) + \hbar \omega_b \hat{b}^\dagger \hat{b} + \hat{\mathcal{H}}_d. \quad (\text{S23})$$

Keeping only first-order terms in the interaction and using the definitions $\hat{\phi} = \phi_{zpf}(\hat{a} + \hat{a}^\dagger)$ and $\phi_{zpf} = (2E_C/E_J)^{1/4}$ we arrive at the Hamiltonian based on creation and annihilation operators. The Hamiltonian can be written in the form,

$$\hat{\mathcal{H}}/\hbar = \omega_q \hat{a}^\dagger \hat{a} + \frac{\alpha}{2} \hat{a}^\dagger \hat{a}^\dagger \hat{a} \hat{a} + \omega_b \hat{b}^\dagger \hat{b} + \frac{\tilde{g}_0}{2} \left(\frac{2E_C}{E_J} \right)^{1/2} (\hat{a} + \hat{a}^\dagger)^2 (\hat{b} + \hat{b}^\dagger) + \hat{\mathcal{H}}_d/\hbar. \quad (\text{S24})$$

Where, we will define $g_0 = \tilde{g}_0 (2E_C/E_J)^{1/2}$. Moreover, the drive Hamiltonian can be written in the form,

$$\hat{\mathcal{H}}_d = \hbar \epsilon_d (\hat{a} e^{i\omega_d t} + \hat{a}^\dagger e^{-i\omega_d t}) \quad (\text{S25})$$

Here, $\epsilon_d = \sqrt{P \kappa_e / \hbar \omega_d}$ is the coherent drive strength. We can now transform the Hamiltonian into a frame rotating at the drive frequency using the unitary transformation $\hat{U} = e^{i\omega_d \hat{a}^\dagger \hat{a} t}$, where $\hat{\mathcal{H}}_{\text{rot}} = \hat{U} \hat{\mathcal{H}} \hat{U}^\dagger + i\hbar (d\hat{U}/dt) \hat{U}^\dagger$, keeping only co-rotating terms we can express the new Hamiltonian as

$$\hat{\mathcal{H}}/\hbar = -\Delta_q \hat{a}^\dagger \hat{a} + \frac{\alpha}{2} \hat{a}^\dagger \hat{a}^\dagger \hat{a} \hat{a} + \omega_b \hat{b}^\dagger \hat{b} + g_0 \hat{a}^\dagger \hat{a} (\hat{b} + \hat{b}^\dagger) + \epsilon_d (\hat{a} + \hat{a}^\dagger). \quad (\text{S26})$$

Here $\Delta_q = \omega_d - \omega_q$. We can first study the steady-state classical dynamics of the Kerr oscillator. The classical equation of motion is given by

$$\frac{d}{dt} \langle \hat{a} \rangle = (i\Delta_q - \gamma_q/2) \langle \hat{a} \rangle - i\alpha |\langle \hat{a} \rangle|^2 \langle \hat{a} \rangle - i g_0 (\langle \hat{b} \rangle + \langle \hat{b}^\dagger \rangle) \langle \hat{a} \rangle - \epsilon_d. \quad (\text{S27})$$

The coupling to the linear resonator mode has the effect of modifying the Kerr nonlinearity as described in⁵², with an effective Kerr nonlinearity of

$$\alpha_{\text{eff}} = \alpha - \frac{2g_0^2 \omega_b}{\omega_b^2 + \gamma_b^2/4}. \quad (\text{S28})$$

Where γ_b is the linewidth of the linear mode. Using the parameters from our device, the correction to the Kerr nonlinearity is much less than the Kerr nonlinearity. Therefore, the equation of motion can be written in the form,

$$\frac{d}{dt} \langle \hat{a} \rangle = (i\Delta_q - \gamma_q/2) \langle \hat{a} \rangle - i\alpha |\langle \hat{a} \rangle|^2 \langle \hat{a} \rangle - \epsilon_d. \quad (\text{S29})$$

In steady-state (i.e. $\langle \dot{\hat{a}} \rangle = 0$), the cubic equation has one real root, but for a large enough input drive, a bistable regime exists. The cubic equation has the form,

$$\bar{n}_q (-\Delta_q + \alpha \bar{n}_q)^2 - \epsilon_d^2 = 0. \quad (\text{S30})$$

Here, we have defined $\bar{n}_q = |\langle \hat{a} \rangle|^2$ the steady-state amplitude of the Kerr oscillator.

C. Photon Number Calibration

To calibrate the number of photons in the qubit due to the sideband drive tone, we use the AC-Stark shift. The driving term applied on the red sideband results in an AC-Stark shift of the Kerr oscillator. Since the drive tone detuning is large ($\Delta_q = \omega_d - \omega_q \approx \omega_b = 4.35$ GHz), we must consider the Bloch-Siegert shift due to the counter-rotating terms, which is described in Ref.²⁷. The AC-Stark shift considering the co- and counter-rotating terms is given by,

$$\delta\omega_q = \frac{1}{2}\epsilon_d^2\alpha\left(\frac{1}{\Delta_q^2} + \frac{2}{|\Delta_q|\Sigma} + \frac{1}{\Sigma^2}\right). \quad (\text{S31})$$

Where $\Sigma = \omega_q + \omega_d$, α is the transmon anharmonicity and $\epsilon_d = \sqrt{\mathcal{P}\kappa_e/\hbar\omega_d}$. We can re-arrange this equation by writing it in the form,

$$\epsilon_d^2 = \frac{2\delta\omega_q}{\alpha}\left(\frac{1}{\Delta_q^2} + \frac{2}{|\Delta_q|\Sigma} + \frac{1}{\Sigma^2}\right)^{-1}. \quad (\text{S32})$$

Therefore, we can calibrate the average photon number in the Kerr oscillator using the AC-Stark shift. Combining Eq. S30 and Eq. S32, the average photon number can be found by solving the cubic equation,

$$\bar{n}_q(-\Delta_q + \alpha\bar{n}_q)^2 - \frac{2\delta\omega_q}{\alpha}\left(\frac{1}{\Delta_q^2} + \frac{2}{|\Delta_q|\Sigma} + \frac{1}{\Sigma^2}\right)^{-1} = 0. \quad (\text{S33})$$

The first real solution to this equation is the photon population of the Kerr-oscillator, $\langle\hat{a}^\dagger\hat{a}\rangle = \bar{n}_q$. Note that treating the qubit as a two-level system at this step underestimates the sideband population and, therefore, will overestimate g_0 .

IV. LINEARIZED PHOTON-PRESSURE

At this point, to continue our analysis, we aim to linearize the theory about the sideband drive applied to the qubit. From the AC-Stark shift calibration above, we found that for all drive powers, the average occupancy $|\langle\hat{a}\rangle|^2$ is much less than a single photon on average. Therefore, we will perform our analysis assuming a harmonic oscillator, making the two-level approximation once we have arrived at a linearized theory.

A. Photon-Pressure Linearization

If we begin with the Hamiltonian given by Eq. S24, rewriting it in the form,

$$\hat{\mathcal{H}}/\hbar = \omega_q\hat{a}^\dagger\hat{a} + \frac{\alpha}{2}\hat{a}^\dagger\hat{a}^\dagger\hat{a}\hat{a} + \omega_b\hat{b}^\dagger\hat{b} + \frac{g_0}{2}(\hat{a}^2 + (\hat{a}^\dagger)^2 + 2\hat{a}^\dagger\hat{a} + 1)(\hat{b} + \hat{b}^\dagger) + (\epsilon_d^*\hat{a}e^{i\omega_d t} + \epsilon_d\hat{a}^\dagger e^{-i\omega_d t}). \quad (\text{S34})$$

In the experimentally relevant situation where the sideband drive is always weak such that $|\langle\hat{a}\rangle|^2 \ll 1$, we will drop the Kerr term as the Kerr oscillator is well approximated by a harmonic oscillator in this weak driving regime. This results in the Hamiltonian

$$\hat{\mathcal{H}}/\hbar = \omega_q\hat{a}^\dagger\hat{a} + \omega_b\hat{b}^\dagger\hat{b} + g_0\hat{a}^\dagger\hat{a}(\hat{b} + \hat{b}^\dagger) + (\epsilon_d^*\hat{a}e^{i\omega_d t} + \epsilon_d\hat{a}^\dagger e^{-i\omega_d t}). \quad (\text{S35})$$

We can simultaneously transform into a frame rotating at the drive frequency and displaced by the steady-state amplitude $\langle\hat{a}\rangle$. This is equivalent to applying the unitary $U = e^{i\omega_d\hat{a}^\dagger\hat{a}t}e^{\langle\hat{a}\rangle^*\hat{a} - \langle\hat{a}\rangle\hat{a}^\dagger}$. The resulting Hamiltonian in the transformed frame is

$$\hat{\mathcal{H}}/\hbar = -\Delta_q\hat{a}^\dagger\hat{a} + \omega_b\hat{b}^\dagger\hat{b} + g_0(\langle\hat{a}\rangle^*\hat{a} + \langle\hat{a}\rangle\hat{a}^\dagger)(\hat{b} + \hat{b}^\dagger) + g_0\hat{a}^\dagger\hat{a}(\hat{b} + \hat{b}^\dagger). \quad (\text{S36})$$

This transformation has separated the photon-pressure interaction into its linear and non-linear components. In this way, we have *only* performed unitary transformations resulting in static shifts of the qubit's equilibrium frequency. Moreover, the last term in this Hamiltonian results in a non-linear two-photon interaction, as described in Ref.²⁰. This term can be dropped since it does not affect the dynamics in the frame of our sideband drive. However, this

term is crucial for generating Schrodinger cat states via the non-linearity of the parametric interaction. We can write our Hamiltonian in the simplified form,

$$\hat{\mathcal{H}}/\hbar = -\Delta_q \hat{a}^\dagger \hat{a} + \omega_b \hat{b}^\dagger \hat{b} + g(\hat{a} + \hat{a}^\dagger)(\hat{b} + \hat{b}^\dagger). \quad (\text{S37})$$

We define the enhanced photon-pressure coupling rate as $g = |\langle \hat{a} \rangle|g_0$ and have assumed it is real. Performing the RWA and approximating the harmonic oscillator as a two-level system, we can write the final Hamiltonian as,

$$\hat{\mathcal{H}}/\hbar = -\frac{\Delta_q}{2} \hat{\sigma}_z + \omega_b \hat{b}^\dagger \hat{b} + g(\hat{\sigma}_+ \hat{b} + \hat{\sigma}_- \hat{b}^\dagger). \quad (\text{S38})$$

We arrive at the photon-pressure Jaynes-Cummings Hamiltonian. Following standard quantum optics techniques⁵³, one can derive the N excitation Rabi frequency given by $2g_N = 2\sqrt{N}g$.

B. Normal-Mode Spectrum

Considering the Hamiltonian given in Eq. S38, we can derive the eigenfrequencies to fit the normal-mode spectra. If we consider the quantity $\hat{N} = \hat{a}^\dagger \hat{a} + \hat{\sigma}_+ \hat{\sigma}_-$ which defines the total number of excitations within the system, in the absence of decay. We notice that $[\hat{\mathcal{H}}, \hat{N}] = 0$, thus is a conserved quantity of the system. Therefore, we can consider the block-diagonal element of the Hamiltonian defined by the total number of excitations spanning the subspace $\{|g, n\rangle, |e, n-1\rangle\}$. This block diagonal element can be written in the form,

$$\hat{\mathcal{H}}/\hbar = \begin{pmatrix} -\Delta_{qb} + n\omega_b & g\sqrt{n} \\ g\sqrt{n} & n\omega_b \end{pmatrix}. \quad (\text{S39})$$

Where $\Delta_{qb} = \omega_b + \Delta_q$, recalling that in the rotating frame $\Delta_q = \omega_d - \omega_q \approx -\omega_b$; therefore, this is the qubit-linear resonator detuning in the rotating frame. Following some algebra, it can be shown that the energy eigenvalues of this block diagonal Hamiltonian have the form³⁸,

$$E_{n,\pm} = n\hbar\omega_b - \hbar \frac{\Delta_{qb}}{2} \pm \frac{\hbar}{2} \sqrt{\Delta_{qb}^2 + 4ng^2}, \quad (\text{S40})$$

from which we can recover the n -quanta Rabi frequency $2g_n = 2\sqrt{ng}$. If we consider the lowest energy manifold of the Jaynes-Cummings ladder, we can determine the expected spectroscopic eigenfrequencies. For $n = 1$, we find the frequency spectrum given by,

$$\omega_{\pm} = \omega_b - \frac{\Delta_{qb}}{2} \pm \frac{1}{2} \sqrt{\Delta_{qb}^2 + 4g^2}. \quad (\text{S41})$$

This can be written in the more enlightening form,

$$\omega_{\pm} = \frac{\omega_b - \Delta_q}{2} \pm \frac{1}{2} \sqrt{\Delta_{qb}^2 + 4g^2}. \quad (\text{S42})$$

Using Eq. S42, we can fit the experimental data to extract g as a function of sideband drive power, as shown in the main text Fig. 2. Using the extracted value of g and the photon number extracted from Eq. S33, we can determine the single-photon coupling rate g_0 , as shown in the main text. It is important to note that this solution *only* holds when the system is within the lowest energy manifold of the Jaynes-Cummings ladder.